Analysis on microseismic characteristics and stability of the access tunnel in the main powerhouse, Shuangjiangkou hydropower station, under high in situ stress

Zhengzhao Liang[1] · Ruixiong Xue[1] · Nuwen Xu[2] · Linlu Dong[2] · Yinghao Zhang[3]

Abstract

Access tunnel in the main powerhouse of Shuangjiangkou hydropower station was deep buried with high in situ stress and complex geological conditions. Microseismic monitoring technology was established to monitor microcrack evolution process inside the surrounding rock in early excavation stage. Serious falling blocks in the left spandrel of the tunnel were predicted in a timely manner by delimiting major damage areas in the tunnel. Based on comparative analysis on microseismic activity law and field failure characteristics of the access tunnel, a quantitative index was supposed between slight rockburst like falling blocks and microseismic events. Moreover, the change law of daily average apparent stress difference and b value were analyzed based on microseismic event data. In addition, a three-dimensional numerical simulation software (RFPA3D) was used to simulate the damage distribution around the tunnel, and a relationship between spatial position of tunnel damage and direction of the maximum principal stress was qualitatively analyzed. The study results showed that advance speed of the tunnel working face was an important factor affecting the state of stress redistribution in surrounding rock mass, and the change law of b values of microseismic events could be used to predict activity state inside the surrounding rock effectively, which reflected mechanical properties and stress state of surrounding rock. In particular, field falling blocks became more serious with increasing b value, and field surrounding rock was relatively stable with minor b value. A risk of surrounding rock instability was relatively high with small b values. It provided an efficient method of predicting and assessing slight rockburst like falling blocks. The study results can provide significant guidance for field construction and later construction planning.

Keywords High in situ stress · Microseismic monitoring · b value · Apparent stress · Numerical simulation

Introduction

A large number of hydropower stations are under construction and scheduled to be constructed in the southwest of China. However, the geological environment is complex in this region. In particular, in environments with great buried depth and high stress, excavation will change the initial stress and energy state of the rock mass, thus initiating a series of geological disasters in the surrounding rock, such as surrounding rock damage, rockburst, and large deformation (He et al. 2005; Xiao et al. 2016), and posing a potential risk to safety of personnel and equipment. Unlike areas under conventional stress, those under high in situ stress and with large buried depth have complex stress conditions and high unloading strength. Excavation in those areas will cause a great impact on the rock mass.

Under high in situ stress, excavation of an underground tunnel is a complex process including rock mass strength deteriorating, rock mass deformation rebounding, and driving fracture expansion in the disturbed rock mass by high in situ stress. Rock bulking may occur as a result of seismic events and does not have to be accompanied by ejection; when this type of failure occurs rapidly, it is typically referred to as a strain rockburst (Kaiser et al. 1996). Seismically induced falls of rock are gravity-driven failures; when a stable volume of

✉ Zhengzhao Liang
LiangZZ@dlut.edu.cn

[1] State Key Laboratory of Coastal and Offshore Engineering, Dalian University of Technology, Dalian 116024, China

[2] State Key Laboratory of Hydraulics and Mountain River Engineering, Sichuan University, Chengdu 610065, Sichuan, China

[3] China Gezhouba Group No.1 Engineering Co Ltd, Yichang 443002, China

rock is subjected to a seismic wave, it is likely to fall (Kaiser et al. 1996). Rock ejection from seismic energy transfer is a more violent damage type; it occurs when the energy resulting from the seismic wave is transferred to a block at the boundary of an excavation (Kaiser et al. 1996). Dong et al. (2014) classified the failure of surrounding rock into gravity-driven controlled by rock mass structure, stress-driven, and compound-driven modes based on the controlling factors.

As the rock mass is disturbed by stress like strong excavation unloading, stress inside the rock mass will be redistributed, thus forming stress concentration zones and stress relaxation zones. Besides, mechanical state of surrounding rock near the free face deteriorates so that microcracks appear inside surrounding rock and the stored elastic energy is released in the stress wave form, thus causing microseismic events (Wang et al. 2008). Three-dimensional microseismic monitoring technology is used to capture microseismic events by deploying a microseismic monitoring system. In this way, parameters pertaining to microcracks are inverted by analyzing microseismic events, including the occurrence time, position, magnitude, etc. in order to assess rock mass stability. Compared with traditional monitoring technology, the microseismic monitoring technology has advantages like long-distance monitoring, three-dimensional monitoring, overall monitoring, and real-time monitoring (Jiang et al. 2002; Cheng et al. 2017). The aggregation and evolution law of microseismic events can well reflect tunnel's construction dynamics and provide early warning precursor information for damage risks of tunnels surrounding rock during the excavation unloading process. Due to high stress field and complex geological conditions in the southwest, the microseismic monitoring technology is widely applied in the construction of large-scale hydropower stations in this area. Feng et al. (2012) analyzed the evolution mechanism of rockbursts at Jinping-II hydropower station and classified them into the immediate rockburst and the time delayed rockburst based on the occurrence time. Zhang et al. (2012) analyzed the stability of the vault collapse area based on microseismic monitoring data of the underground caverns at Dagangshan hydropower station. Xu et al. (2014) analyzed the relationship between the distribution of microseismic events and slope stability by installing the ESG microseismic monitoring system on the slope of Jinping-I hydropower station. Liu et al. (2017) deployed the microseismic monitoring system at Dagangshan hydropower station to conduct microseismic monitoring on the slope during reservoir impounding.

In spite of many studies from domestic and foreign scholars on the damage types of underground tunnels and application of the microseismic monitoring technology under hydropower station construction, many issues need to be further studied due to different geological environments of construction fields and complex practical problems. In projects, it is difficult to predict and assess slight rockbursts like falling blocks, and no

appropriate assessing methods are available. However, slight rockbursts can similarly do serious harm to the field, and how to fully mine microseismic monitoring data to obtain more useful information needs to be further studied.

Taking the access tunnel in the main powerhouse of Shuangjiangkou hydropower station as the research object, we aimed to resolve some stability problems like large-area falling blocks of surrounding rock in the left spandrel of the tunnel. Based on existing data of microseismic monitoring, we analyzed daily average apparent stress (DAAS) difference and b values of microseismic events and summarized the relationship between their change characteristics and activities of field surrounding rock. Moreover, we found that secondary stress distribution of surrounding rock was closely related to advance speed of working faces and that b values change law could predict activity state inside tunnel surrounding rock and reflect physical and mechanical properties and stress state of surrounding rock. We provided an effective method of predicting and assessing slight rockbursts like falling blocks. In addition, we further applied the RFPA3D finite element numerical simulation software to simulate and reproduce the field situation and analyze damage mechanism of the tunnel surrounding rock.

Project overview and geological conditions

The Shuangjiangkou hydropower station constructed on the Dadu River is located approximately 382 km northwest of Chengdu in Sichuan Province, China. It is developed mainly for electricity generation. The project is constructed in a V-shaped valley, includes a 314-m-tall soil core rockfill dam which is the world's tallest dam in the same type of dam, and controls a drainage area of more than 39,330 km^2. The reservoir has a normal pool level of 2500 m. The total storage capacity is 2.897 billion m^3, and the adjustment storage capacity is 1.917 billion m^3. The powerhouse can accommodate four 500 MW turbine generators for a total generating capacity of 2000 MW.

The entrance of the access tunnel in the main powerhouse locates at the upstream of the Feishuiyan stream. Total length of the tunnel is 1473.31 m, and cross-sectional dimensions are 11.24 m × 8.7 m (width × height), as shown in Fig. 1a. Bottom of the tunnel is located at elevations of 2253.00 m. Figure 1b shows a geological profile of the tunnel. The main rock type of the tunnel is biotite K-feldspar granite which has a uniaxial compressive strength of 60–70 MPa. The rock mass is mainly blocky with a moist tunnel wall and even drips of water in the local. As the surrounding rock is mainly made of class IIIa, after the deduction of high in situ stress, overall stability of the tunnel wall is satisfactory. A deep-buried tunnel section under high in situ stress has the largest vertical buried depth up to 600 m. Affected by weathering and unloading, the entrance superficial rock

Fig. 1 Left bank slope of Shuangjiangkou hydropower station. **a** Photograph of the left bank showing geological conditions and outline drawing of the access tunnel in the main powerhouse. **b** Geological profile of the access tunnel in the main powerhouse
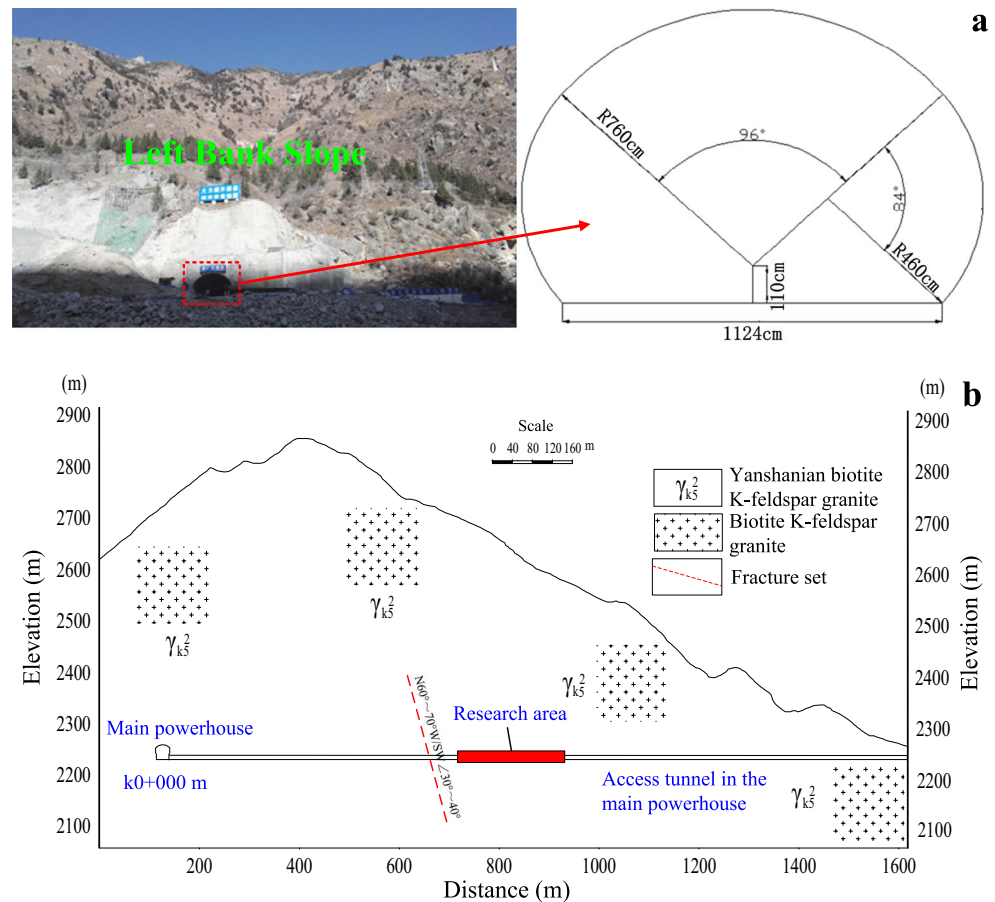
mass has bad local stability, and local low-angle dip structural plane is bad for the stability of vault surrounding rock. Based on the measured in situ stress of adit SPD9 that is an exploratory tunnel excavated before the underground tunnel is excavated, with entrance elevation of 2267.6 m, the maximum principal stress σ_1 ranges from 15.98 to 37.82 MPa, belonging to the high stress level.

Microseismic monitoring

Microseismic monitoring system architecture

A high-sensitivity microseismic monitoring system, manufactured by the Engineering Seismology Group (ESG), Canada, was installed at the access tunnel in the main powerhouse, as shown in Fig. 2. Based on the field construction conditions of the access tunnel and the best monitoring effects of accelerometers, the microseismic monitoring system consists of a Paladin digital signal acquisition system, a Hyperion digital signal processing system, six uniaxial accelerometers, and signal transmission cables, forming a network structure in the spatial area. The cables from all accelerometers were connected to a Paladin acquisition unit. The Paladin data acquisition system,

using the STA/LTA algorithm with a threshold of 3, has an acquisition frequency of 20 kHz and a 24-bit analog-to-digital (A/D) converter. The accelerometers respond to frequencies in the range from 50 to 5 kHz, with a sensitivity of 30 V/g.

The accelerometers were cemented in the boreholes at the sidewalls using quick-hardening resin. The boreholes were 42 mm in diameter. To decrease disturbance of background noise, boreholes were no less than 2 m in depth. According to the on-site construction conditions of the access tunnel in the main powerhouse and the optimum monitoring range of accelerometers, six accelerometers were installed in three different cross sections, and the interval of the accelerometers along the tunnel axis was 40 m, as shown in Fig. 2. When no less than four accelerometers were triggered, the location of the seismic source can be determined (Liu et al. 2019). When the working face was advanced for approximately 40 m, the last row of accelerometers was moved forward to become the first row. To ensure the safety of personnel and microseismic monitoring equipment, the first row of accelerometers was designed to be no less than 50 m behind the working face. To continuously capture the excavation unloading-induced microcracks within the surrounding rock mass, the first row of accelerometers was designed to be no more than 100 m behind the working face.

Fig. 2 Topology of the microseismic monitoring system
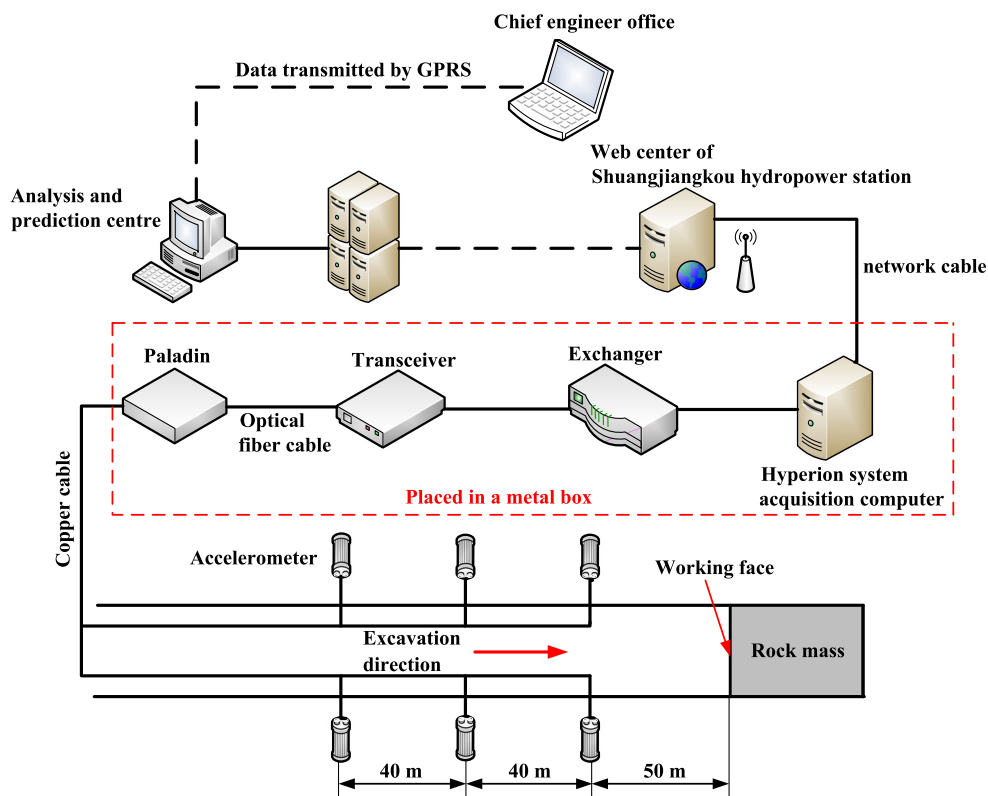
Microseismic activity law and field failure characteristics

This project lasted from September 1, 2017, to December 21, 2017, during which a total of 964 effective microseismic events were detected. Figure 3 shows distribution of microseismic events with different location errors, among which events with the location error less than 10 m accounted for 73.86% (Tang et al. 2018), indicating that monitoring data
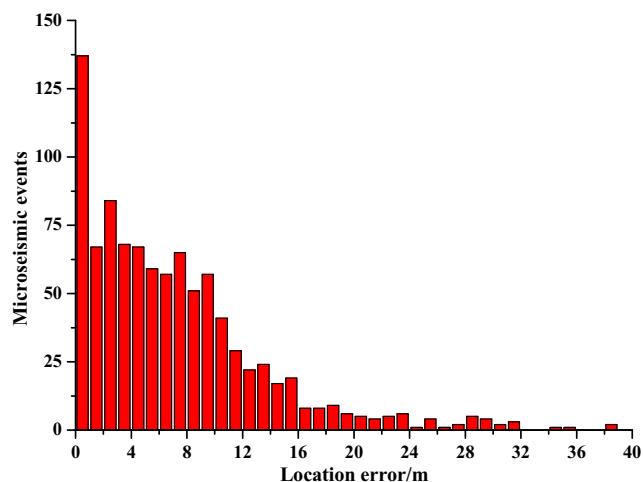

Fig. 3 Distribution of microseismic events location error

could fully meet demand for assessing the stability of the tunnel surrounding rock. Figure 4 shows the daily number of events. In particular, microseismic events occurred most frequently on October 11 and October 22, with the event number up to 32 and 31, respectively; the total number of events occurring from October 2 to November 2 reached 389, accounting for 40.35% of the total (Fig. 4). That indicated frequent microseismic activities and serious falling blocks. Specifically, length of the tunnel with continuous falling blocks was over 150 m, and an about 60-m-long crack appeared from excavation Chainage k0 + 860 m to k0 + 800 m, seriously affecting construction progress and safety of the field personnel and equipment. The total number of events occurring from November 24 to December 9 reached 199, accounting for 20.64% of the total (Fig. 4), which indicated relatively frequent microseismic activities inside the tunnel surrounding rock. Moreover, an about 50-m-long crack appeared from Chainage k0 + 660 m to k0 + 610 m. Therefore, two periods with frequent microseismic activities were selected in this paper to analyze the relationship between microseismic activities and surrounding rock damage.

Excavation unloading changes stress environment of the tunnel surrounding rock and deteriorates physical and mechanical properties of surrounding rock. The stress inside the rock mass needs to be redistributed to achieve a balance. Microcracks will appear when acting force exceeds the

Fig. 4 Time-frequency distribution of microseismic events
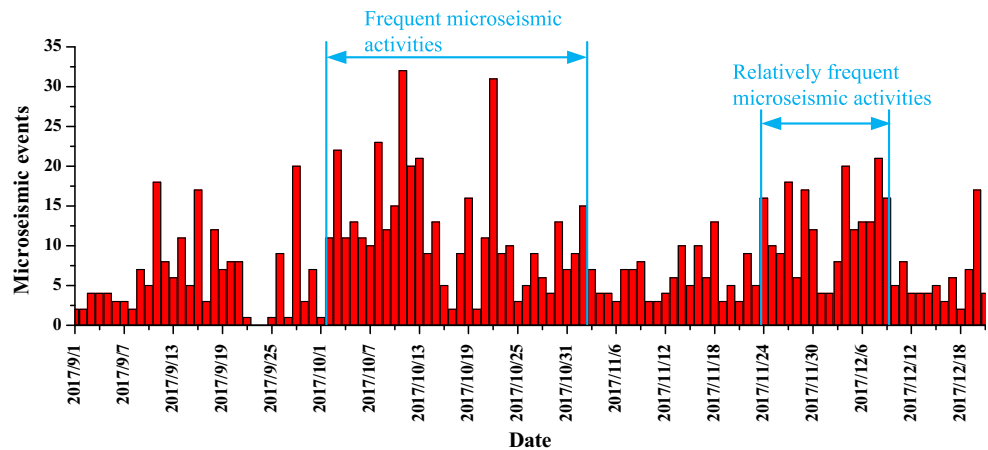
strength of the surrounding rock, eventually causing elastic energy accumulating in the rock mass to release (Zhou et al. 2018; Feng et al. 2019). A density cloud chart of microseismic events can vividly reveal concentrating area of microcracks inside the tunnel surrounding rock. Figure 5 shows density cloud charts of microseismic events occurring from October 2 to November 2, during which microseismic events were frequent overall. On October 2, 2017, the number of microseismic events was 11; the number reached 22 on October 3; the number remained at a relatively high level for several days. On October 4, it was found that field rock spalling and falling blocks intensified and continued to increase. Due to serious field falling blocks, excavation progress was slowed and even terminated until the surrounding rock became stabilized from October 14. After November 2, the surrounding rock of the tunnel became stabilized.

A drilling and blasting method was adopted to construct the access tunnel in the main powerhouse. When the tunnel working face was blasted, the tunnel surrounding rock was disturbed by blasting excavation, consequently changing stress state and deteriorating mechanical state. At this time, the rock mass was prone to microcracks, and microseismic activity was in the active period. If large cracks appeared in the surrounding rock, the number of microseismic events would increase sharply. After comparative analysis on the microseismic activity law and field damage characteristics, we found that when the number of microseismic events reached 15, the field falling blocks were slight and that when the number was over 20, the field falling blocks were serious. When stress was readjusted to balanced state, activities inside the surrounding rock weakened or terminated, which was a quiet period of microseismic events. Therefore, in terms of spatial distribution, microseismic events were generally active near the working faces; in terms of temporal distribution, microseismic events were generally active just after blasting. Consequently, with the advance of excavation, disturbed part of the rock mass was gradually pushed forward, and microseismic events gradually appeared in the new disturbed area of excavation, as shown in Fig. 5. It could

be found from Fig. 5a, b, and c that the damage area of surrounding rock expanded constantly with the advance of excavation. It could be found from Fig. 5d that microseismic events were mainly concentrated in the left spandrel of the tunnel, followed by the right arch foot. Accordingly, the density of events occurring in the right arch foot was lower than that of events occurring in the left spandrel. The damage degree of the tunnel surrounding rock caused by blasting excavation could be well identified from Fig. 5. It was found that an area with the most frequent microseismic activities was the left side of the tunnel with Chainage from k0 + 812 m to k0 + 830 m.

Figure 6 shows failure characteristics of field surrounding rock. The damage in the left spandrel of the tunnel was mainly classified into three forms: serious damage area (V-shaped damage area), slight falling blocks area (nest-shaped damage area), and cracks. The damage in the right arch foot was relatively minor. Based on microseismic monitoring and field investigation, it was found that damage type of the access tunnel in the main powerhouse was classified into the microseism-induced and gravity-driven type.

Figure 7 shows density cloud charts of microseismic events in the second period from November 24 to December 9. From November 24, 2017, the number of microseismic events continued to maintain a relatively high level. Especially on December 4 and December 8, the number of events reached 20 and 21, respectively, indicating frequent microseismic activities. According to the field investigation, on December 4 and the following days, falling blocks occurred seriously and cracks appeared, as shown in Fig. 8.

It could be found from comparative analysis on the density cloud charts of microseismic events and field investigation that two sections of tunnel falling blocks occurred in the same part of the tunnel: serious damage in the left spandrel and slight damage in the right arch foot. Compared with the first period, field falling blocks were mitigated in the second period. However, it still made a considerable impact on the field construction progress and safety of personnel and equipment. Therefore, it was necessary to conduct source multiparameters
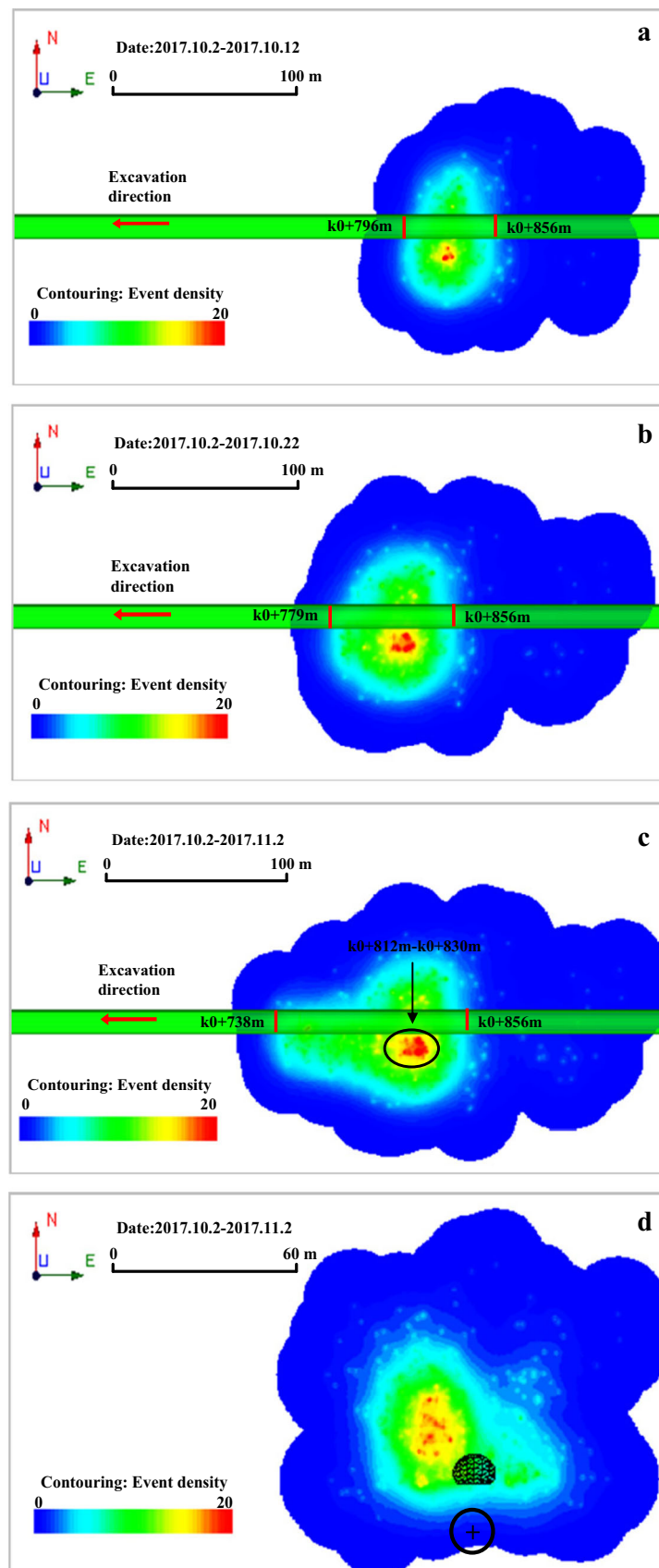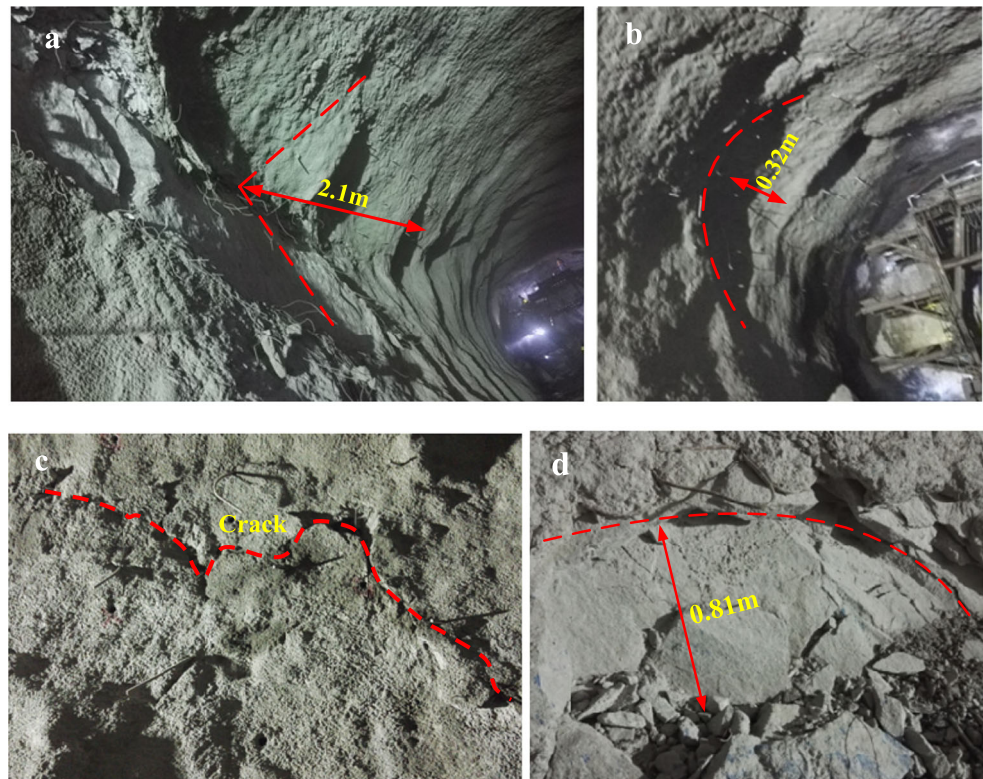
Fig. 5 Density cloud charts of microseismic events (top views a, b, and c, profile d)

Fig. 6 Damage photographs of the field surrounding rock. **a** Serious damage area (left spandrel). **b** Slight falling blocks area (left spandrel). **c** Crack area (left spandrel). **d** Right arch foot damage area

analysis in combination with the numerical simulation method, to accurately estimate and verify the temporal and spatial distribution of the tunnel falling blocks and further reveal the mechanism of microseismic events under excavation disturbance, so as to ensure safety of field personnel and equipment and provide a guidance for the field construction progress and later planning.

Analysis of apparent stress and *b* values

Apparent stress

As an important parameter in the process of earthquake preparation, apparent stress is often used to describe the change law of the rock mass before and after an earthquake, and it is not limited by the selected source models. The larger the apparent stress fluctuation, the stronger the disturbance caused by excavation. A sharp increase or decrease in the apparent stress is the precursor of a rockburst. Therefore, apparent stress differences can be used to express dynamic law of the surrounding rock, as shown in Fig. 9. Wyss et al. (2012) concluded through research that the seismic apparent stress can be expressed as follows:

$$\sigma_A = \eta \sigma \tag{1}$$

where σ_A is the apparent stress, η is the seismic efficiency defined as the fraction of the total energy that is radiated

seismically, and σ is the average stress acting on the fracture surface when microcracks appear in the rock mass. The daily average apparent stress (DAAS) is expressed as follows:

$$\overline{\sigma}_A = \frac{\sum \sigma_A}{N} \tag{2}$$

The DAAS difference can be expressed as:

$$\Delta \overline{\sigma}_A = \overline{\sigma}_A^{n+1} - \overline{\sigma}_A^{n} \tag{3}$$

where $\overline{\sigma}_A$ is the DAAS, $\sum \sigma_A$ is the sum of daily apparent stress, N is the number of daily microseismic events, $\Delta \overline{\sigma}_A$ is the DAAS difference, $\overline{\sigma}_A^{n+1}$ is the DAAS on day n + 1, and $\overline{\sigma}_A^{n}$ is the DAAS on day n. Positive values of the apparent stress difference mean increasing stress on the rock mass, while negative values of the apparent stress difference mean that rock mass releases stress through damage.

Figure 9 shows the relationship between DAAS difference and daily average excavation speed in two periods. In the first period, the DAAS increased considerably on October 17, October 26, October 30, and November 1, indicating that the rock mass stress redistribution was active during this period. In combination with field analysis, it was found that the DAAS difference was closely connected with the blasting excavation speed. Due to serious field falling blocks before October 16, 2017, the excavation speed was slow, with an about 1.5 m/day advance speed of the working face.

Fig. 7 Density cloud charts of microseismic events (top view a, profile b)
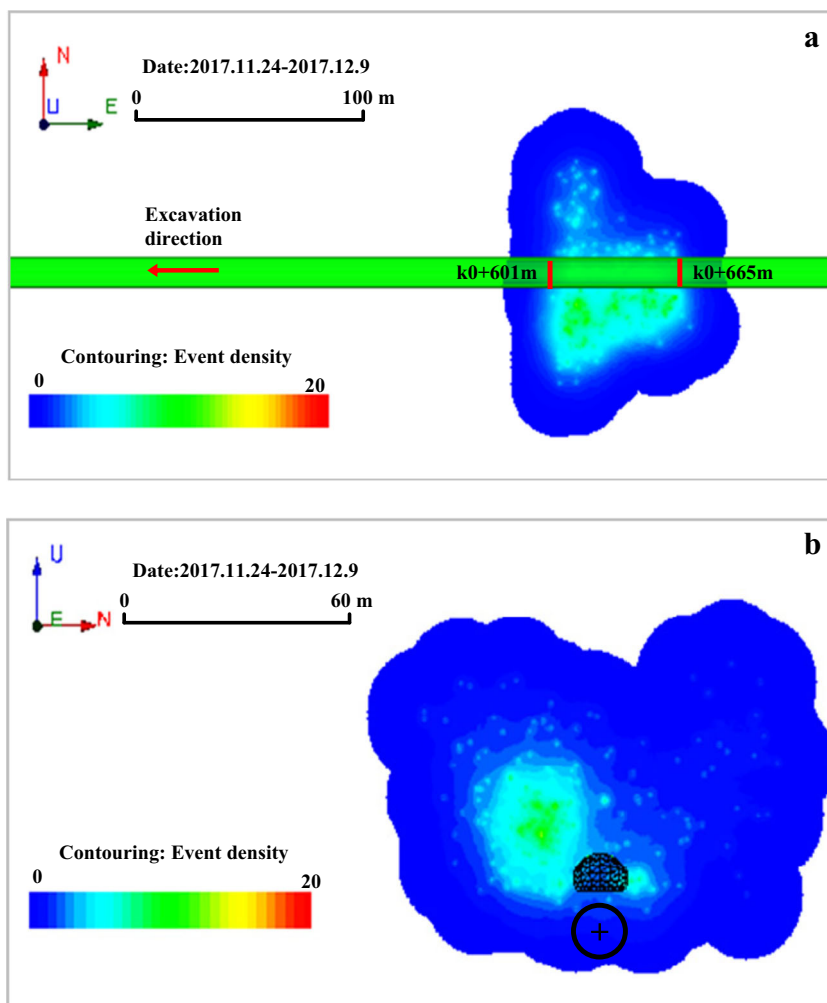
However, from October 16 to November 2, 2017, the excavation speed was fast, with an about 4 m/day advance speed of the working face. The surrounding rock stress increased a lot after field excavation speed increased, which fully indicated that advance speed of the working face was one of main factors affecting disturbance on the rock mass. Therefore, appropriately slowing down excavation can effectively reduce slight rockbursts like falling blocks in sections with weak rock mass strength or high in situ stress.
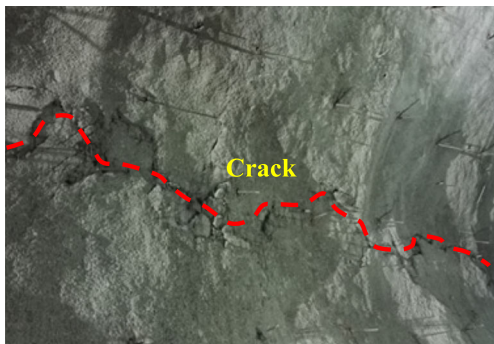

Fig. 8 Damage photograph of field surrounding rock

In the second period, the DAAS increased a lot on November 28 and December 1. From November 24 to December 3, 2017, the advance speed of the working face was fast, reaching about 4.5 m/day; however, from December 3 to December 9, 2017, the advance speed was about 2.5 m/day due to poor tunnel formation. Therefore, a high apparent stress difference was caused by stress concentration due to insufficient release of stress when advance speed of the working face was relatively rapid, which once again fully indicated that the advance speed of the working face was one of main factors affecting disturbance on the rock mass.

Based on comprehensive analysis on Fig. 9, it was found that the DAAS was closely related to the advance speed of the working face. When the average advance speed of the working face was 4.5 m/day, the apparent stress fluctuated considerably, and the risk of surrounding rock instability was relatively high. Thus, engineers were advised to reduce the advance speed of the working face in the case of poor overall stability of surrounding rock or high initial in situ stress. In well-formed sections of the access tunnel in the main

Fig. 9 Relationship between DAAS difference and average excavation speed
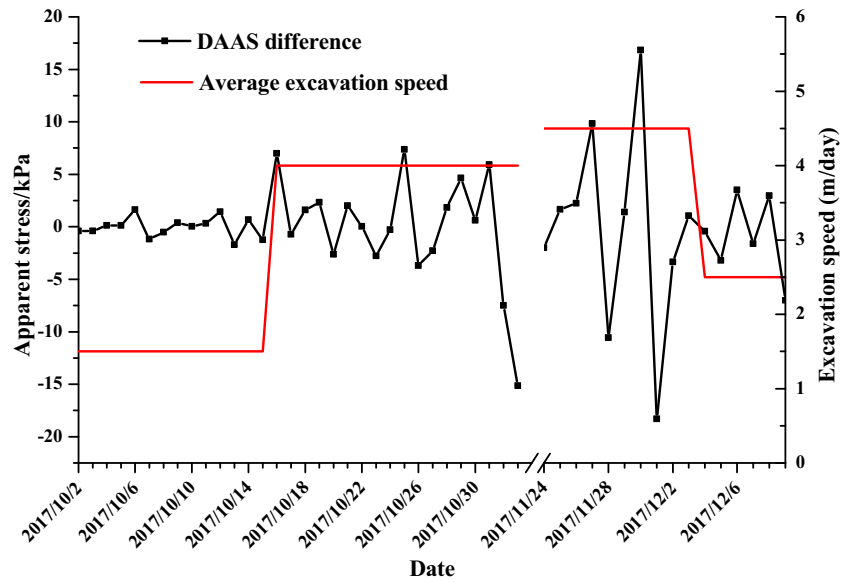
powerhouse of Shuangjiangkou hydropower station, it was suggested that average advance speed of the working face should not be more than 4 m/day. If the advance speed of the working face was too high, the stress could not be released in time and would increase too fast, consequently increasing the risk of surrounding rock instability and affecting later excavation. For example, from November 24 to December 3, 2017, the advance speed of the working face was fast, reaching 4.5 m/day, which caused blocks to fall in the tunnel and affected later excavation, as shown in Fig. 8.

b values analysis

Some research results based on field observations (Liu et al. 2019) show that moment magnitude and frequency of microseismic events also comply with earthquake magnitude-frequency (G-R) relational expression in the earthquake area. An expression showing the statistical relationship between the earthquake magnitude and frequency was put forward by Gutenberg and Richter (1944). The expression is as follows:

$$\lg N = a - bM \qquad (4)$$

where M is the earthquake magnitude, N is the number of earthquakes with the magnitude greater than or equal to M, and a and b are constants. The b value indicates the ratio between the number of events with smaller magnitude and that of events with larger magnitude. The smaller the b value, the greater the proportion of large magnitude events. The change of the b values may be used to reflect the change of stress field. The b values of microseismic activity caused by stress adjustment are generally between 1.2 and 1.5 (Legge et al. 1987).

Since sensor arrays are all located at a certain distance from the source, there is a probability that small-magnitude events fail to be received by the sensors due to relatively high propagation attenuation; the frequency of large-magnitude events is relatively low. Therefore, in order to improve the accuracy of b-value calculation by fitting curve, event groups of intermediate magnitude should be selected. In this paper, in the process of obtaining the b values, curve fitting degree R^2 is greater than 0.96; $\Delta M = 0.1$ MPa. Figure 10a and b show moment magnitude-frequency distribution of microseismic events in the first and second time periods. The b value in the first time period is 1.453; the b value in the second time period is 1.296. The b values in the two time period are between 1.2 and 1.5 (Legge et al. 1987). However, the b value in the first time period is greater than that in the second time period.

In the period from September 1 to December 21, 2017, a total of 964 effective microseismic events were detected. Then, we calculated b values for the 964 microseismic events in the period. To improve the accuracy of b values calculation, this paper took 10 days as a time period for calculating the b values; at least 8 days were used as a time period at both ends to calculate the b values. An initial time for b value calculation of the second time shall be 2 days later than that of the first time. The rest could be done in the same manner. We needed to calculate the b values for five times (except the time at both ends), as shown in Fig. 11. Calculate the b values and fitting degree of each time period, as shown in Table 1; then, we could obtain the b value per day: $b = (b1 + b2 + b3 + b4 + b5)/5$.

When the b value is smaller, the surrounding rock stress is higher; the surrounding rock is at a high risk of instability. Since strength of the tunnel surrounding rock is relatively
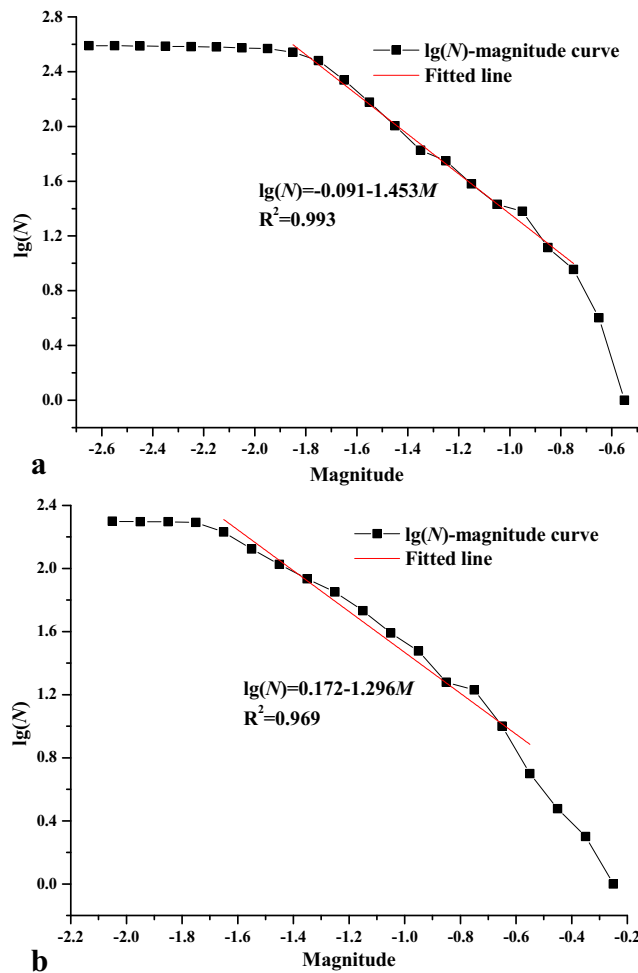
Fig. 10 Moment magnitude-frequency distribution of microseismic events. **a** 2017.10.02~2017.11.2. **b** 2017.11.24~2017.12.09

low and tunnel walls are wet, when the density of microcracks within the surrounding rock is large or falling blocks occur on the field (it is a process of stress release), the magnitude for most events is smaller; b values are larger. When activity intensity of the surrounding rock on the field is smaller (it is also a process of stress accumulation), the b values gradually decrease. Therefore, either larger or smaller b values indicate that the field surrounding rock is at a higher risk of instability.

Fig. 11 b values calculation scheme

Table 1 b values calculation

No.	Date	b values	Fitting degree
$b1$	9.1–9.10	0.74069	$R^2 = 0.97767$
	9.11–9.20	0.9324	$R^2 = 0.96214$
	9.21–9.30	1.566	$R^2 = 0.96354$
	10.1–10.10	1.854	$R^2 = 0.96912$
	10.11–10.20	1.60624	$R^2 = 0.98334$
	10.21–10.30	1.12684	$R^2 = 0.98088$
	10.31–11.9	0.92272	$R^2 = 0.96422$
	11.10–11.19	1.28343	$R^2 = 0.96132$
	11.20–11.29	1.14577	$R^2 = 0.97026$
	11.30–12.09	1.229	$R^2 = 0.98104$
	12.10–12.19	1.26347	$R^2 = 0.98063$
$b2$	9.3–9.12	0.52855	$R^2 = 0.9669$
	9.13–9.22	1.6586	$R^2 = 0.97414$
	9.23–10.2	1.71758	$R^2 = 0.96589$
	10.3–10.12	1.99704	$R^2 = 0.97927$
	10.13–10.22	1.45896	$R^2 = 0.98633$
	10.23–11.1	0.91059	$R^2 = 0.98471$
	11.2–11.11	0.75738	$R^2 = 0.97029$
	11.12–11.21	1.12516	$R^2 = 0.97484$
	11.22–12.1	0.95978	$R^2 = 0.9664$
	12.2–12.11	1.33614	$R^2 = 0.98547$
	12.12–12.21	0.82922	$R^2 = 0.96561$
$b3$	9.5–9.14	0.58736	$R^2 = 0.97165$
	9.15–9.24	1.03125	$R^2 = 0.96633$
	9.25–10.4	1.63864	$R^2 = 0.97413$
	10.5–10.14	1.76113	$R^2 = 0.99392$
	10.15–10.24	1.74281	$R^2 = 0.98491$
	10.25–11.3	1.0096	$R^2 = 0.96501$
	11.4–11.13	0.89223	$R^2 = 0.97692$
	11.14–11.23	1.10544	$R^2 = 0.98153$
	11.24–12.3	0.97559	$R^2 = 0.96496$
	12.4–12.13	1.41415	$R^2 = 0.9805$
	12.14–12.21	0.7238	$R^2 = 0.97751$
$b4$	9.7–9.16	0.72912	$R^2 = 0.96213$
	9.17–9.26	1.11229	$R^2 = 0.9768$
	9.27–10.6	1.55831	$R^2 = 0.98174$
	10.7–10.16	1.75263	$R^2 = 0.98957$
	10.17–10.26	2.04369	$R^2 = 0.99669$
	10.27–11.5	0.97579	$R^2 = 0.96724$
	11.6–11.15	1.0763	$R^2 = 0.96614$
	11.16–11.25	1.0822	$R^2 = 0.97238$
	11.26–12.5	1.1332	$R^2 = 0.96003$
	12.6–12.15	1.38912	$R^2 = 0.98444$
$b5$	9.1–9.8	0.73621	$R^2 = 0.96654$
	9.9–9.18	0.80682	$R^2 = 0.97384$
	9.19–9.28	1.33799	$R^2 = 0.98065$
	9.29–10.8	2.11581	$R^2 = 0.97666$
	10.9–10.18	1.77927	$R^2 = 0.99022$
	10.19–10.28	1.73998	$R^2 = 0.99114$

Table 1 (continued)

No.	Date	b values	Fitting degree
	10.29–11.7	0.79933	$R^2 = 0.97708$
	11.8–11.17	1.01368	$R^2 = 0.96898$
	11.18–11.27	1.00446	$R^2 = 0.97049$
	11.28–12.7	0.96703	$R^2 = 0.99232$
	12.8–12.17	1.46492	$R^2 = 0.9915$

Hence, if the b value curve fluctuation is small, the stability of the surrounding rock is good.

According to Fig. 12 and field comparison, before large-area falling blocks of the access tunnel in the main powerhouse, the b values experienced a trough; the minimum b value was 0.65, which was far less than 1.2; a proportion of large-magnitude events was relatively large; the stress of the surrounding rock of the tunnel was larger; the tunnel surrounding rock was at a higher risk of instability. Then the b value gradually increased until it reached the peak value 1.896 (greater than 1.5) on October 8; it indicated abnormal activity of the tunnel surrounding rock. On October 11, the number of microseismic events reached 32 (maximum value); it was the most serious day for field falling blocks. Then the b values started to go down a little and then rose a little bit to 1.726 on October 18; 4 days later (that was, October 22), the number of events reached 31. Then the b values continued to go down for a long time. After October 23, the degree of tunnel falling blocks was reduced or no falling blocks occurred. On November 9, the b values experienced the second trough and then started to rise again to 1.122 with a smaller increment. In this period, the tunnel was relatively well formed;

almost no falling blocks occurred. On November 25, the b values experienced the third trough and then continuously increased to 1.37 on December 11. In this period, continuous falling blocks occurred in the tunnel, but the degree was relatively slight. Then, the b value went down; field observations showed that the degree of tunnel falling blocks began to ease. The first valley-to-peak difference Δb_1 was 1.248; the second valley-to-peak difference Δb_2 was 0.253; the third valley-to-peak difference Δb_3 was 0.337. According to the change rules of b values with time, the greater the Δb value, the larger the b values fluctuation; field falling blocks were more serious. If the b values were relatively stable, the surrounding rock on the field was relatively stable. If the b values tended to go down, field falling blocks will be mitigated or will not occur. This showed that the change law of b values could be used as an indicator for predicting activity state of field surrounding rock. According to Fig. 12, when the surrounding rock was most seriously damaged on site, the b values were large, and the large b values lasted for a long time. This was related to physical parameters of the field surrounding rock. The category of the surrounding rock for access tunnel in the main powerhouse is mainly IIIa featuring low compressive strength (60 MPa); in addition, the tunnel walls are wet; small-magnitude events predominate in microcracks of the surrounding rock. This showed that the change law of b values could reflect mechanical properties of the surrounding rock. If the b value was small, the proportion of large-magnitude events was relatively large. It indirectly reflected that the surrounding rock stress was high and the surrounding rock was at a higher risk of instability. This point was also proved by continuous falling blocks in the time periods after the b values trough.

Fig. 12 Temporal distributions of event count and b values
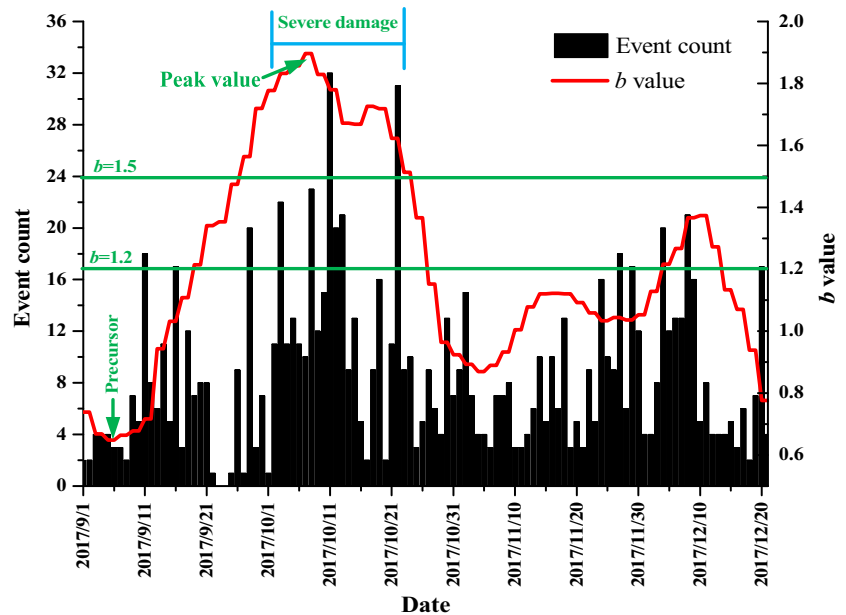
Numerical simulation analysis

To further study damage mechanism of the tunnel, this paper used the RFPA3D finite element analysis software to perform detailed analysis on the field falling blocks mechanism. The calculation range of a 3D model is 100 m × 100 m × 60 m. Segmental excavation of the underground tunnel was simulated. The model adopted the Mohr-Coulomb (M-C) criterion. Table 2 shows physical and mechanical parameters pertaining to the tunnel surrounding rock. The x-axis is perpendicular to the direction of tunnel excavation; the y-axis is the direction of tunnel excavation; the z-axis is vertically down. The ANSYS software was used for modeling with the normal constraints around the computational domain. In the model, in situ stress boundary conditions were obtained after inversion of the measured in situ stress; the maximum initial in situ stress of the rock mass in the engineering area before tunnel excavation is 37.82 MPa. Figure 13 shows a mesh generation of the finite element model. The C programming data-conversion interface program AtoR was used to extract and read ANSYS model data such as nodes and units to the RFPA3D program for analysis of the tunnel stability. The gravity may affect size and orientation of stress; in this paper, to study the law for effects of the principal stress on surrounding rock damage, only the principal stress was applied in the model; the gravity was not applied. In the model, excavation was carried out according to the normal field construction progress: 4 m for each time and 15 times in total. Figure 14 shows operation results of the model. In the acoustic emission figure, red balls indicate compression-shear failure; blue balls indicate tensile failure.

As can be seen from Fig. 14a, after the tunnel excavation, the tunnel surrounding rock is mainly in two stress states from the perspective of mechanical state: stress concentration state and stress relaxation state. In the stress concentration state, the rock mass damage is compression-shear failure; in the stress relaxation state, the tensile effect is generated due to excavation unloading, and the rock mass damage is tensile failure. According to the acoustic emission diagram, the damage of the tunnel surrounding rock was mainly compression-shear failure. The size and orientation of the maximum principal stress led to stress concentration of the left spandrel and right arch foot of the tunnel, as shown in Fig. 14a. Meanwhile, due to blasting excavation, the mechanical state of the surrounding rock mass deteriorated; when the strength of local rock mass
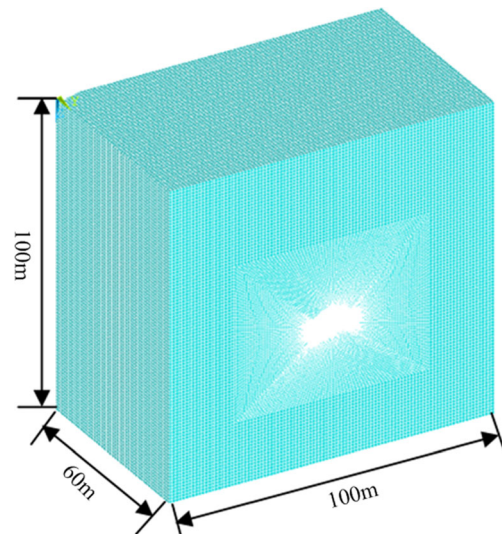

Fig. 13 Finite element model of access tunnel in the main powerhouse

in surrounding rock was smaller than the imposed stress, microcracks occurred; microcracks continued to develop into macroscopic damage, as shown in Fig. 14b; that was, the left

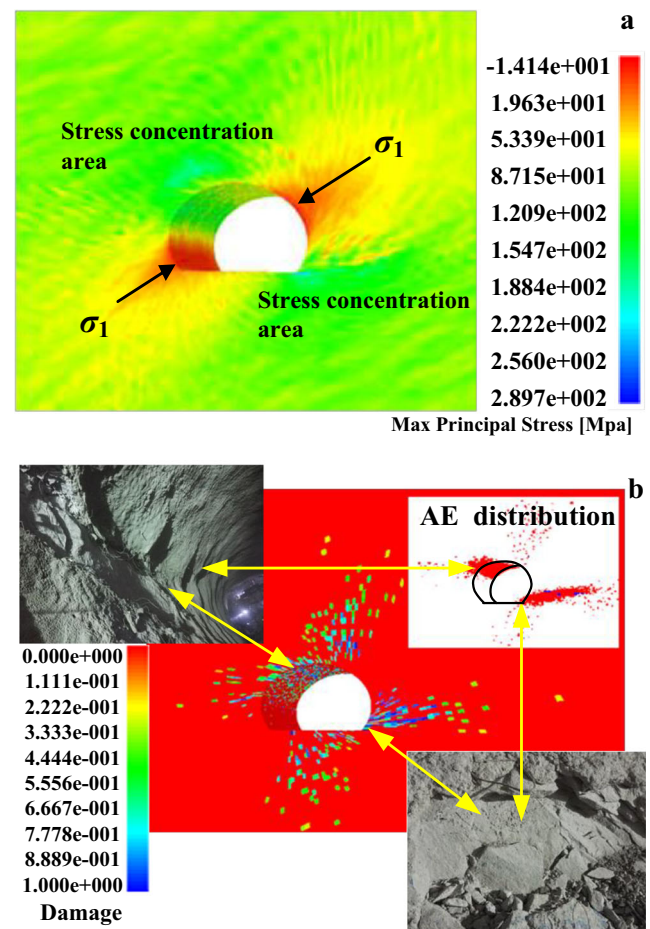Fig. 14 Numerical results after excavation. a Distribution of the maximum principal stress (a negative value represents tensile stress). b Distribution of the damaged elements and acoustic emission

Table 2 Mechanical parameters of intact rocks

Density (kg/m^3)	Elastic modulus (GPa)	Compressive strength (MPa)	Poisson's ratio	Frictional angle (°)
2550	7	60	0.3	40

spandrel and right arch foot of the tunnel were seriously damaged. In actual excavation, the rock mass at the left spandrel of the tunnel would fall off due to gravity; the rock mass close to the free face became the secondary free face; most of damaged rock mass was in free face or near the free face; therefore, the damage was relatively severe. However, the rock mass damage area at the right arch foot took a strip shape and occurred within the rock mass; actually, the damage was relatively minor, as shown in Fig. 6. In the stress relaxation area, part of the rock mass was in the state of tensile stress. However, the tensile stress area is arched; the tensile resistance is strong; therefore, damage to this part of the rock mass was small. Therefore, comprehensive analysis results showed that damage evolution law and damage types in the disturbed area around the tunnel were not only related to the shape and size of the tunnel but also related to the size and orientation of the maximum principal stress. Especially, the size and orientation of the maximum principal stress were the main factors affecting the secondary distribution of the surrounding rock stress.

Conclusion

In this paper, a comparative analysis was performed on the microseismic activity law and field failure characteristics of the access tunnel in the main powerhouse at Shuangjiangkou hydropower station; a quantitative relationship between slight rockbursts such as falling blocks and microseismic events was established. On the basis of abundant source information obtained from microseismic monitoring, the change laws of DAAS differences and b values were analyzed. Specific to spatial distribution characteristics of serious falling blocks in the tunnel, a 3D numerical simulation software (RFPA3D) was used for numerical calculation to analyze damage mechanisms for the tunnel surrounding rock. The main conclusions are as follows:

(1) Microseismic monitoring technology was used to predict spatiotemporal distribution of serious falling blocks in the access tunnel in the main powerhouse; a quantitative relationship between slight rockbursts such as falling blocks and microseismic events was established. According to field investigation, when the number of microseismic events reached 15, slight falling blocks or cracks would generally occur on site; when the number of field events was greater than 20, falling blocks were generally serious on site.

(2) According to the comparison between DAAS differences and field excavation progress, the advance speed of working face was one of important factors affecting the secondary distribution of the surrounding rock stress; meanwhile, the advance speed of working face affected the surrounding rock stability in subsequent tunnel excavation. This

proved that it was one of the most effective measures for ensuring relatively stable surrounding rock to slow down excavation progress when the damage to surrounding rock was serious; this provided guidance for field construction progress. According to the change law of b values with time, the larger the b values fluctuation, the more serious the field falling blocks. If the b values were relatively stable, the surrounding rock on the field was relatively stable. If the b value was small, the surrounding rock was at a higher risk of instability. This shows that this indicator can be used to predict activity state of the field surrounding rock. The change law of b values can also reflect physical and mechanical properties and stress state of the surrounding rock.

(3) The field conditions were simulated and reproduced on the basis of numerical simulation to analyze a relationship between spatial position of tunnel damage and the direction of the maximum principal stress. Thus, a nature that damage to the left spandrel of the tunnel surrounding rock was severe was revealed.

The research results provide certain reference for field construction and later construction planning.

References

Cheng GW, Ma TH, Tang CA, Liu HY, Wang SJ (2017) A zoning model for coal mining-induced strata movement based on microseismic monitoring. Int J Rock Mech Min Sci 94:123–138

Dong JX, Xu GL, Li ZP, Song SW, Zhang SS, Xiao PX, Zhang FT, Shen YJ (2014) Classification of failure modes and controlling measures for surrounding rock of large-scale cavers with high geostress. Chin J Rock Mech Eng 33(11):2161–2170 (In Chinese)

Feng XT, Chen BR, Li SJ, Zhang CQ, Xiao YX, Feng GL, Zhou H, Qiu SL, Zhao ZN, Yu Y, Chen DF, Ming HJ (2012) Studies on the evolution process of rockbursts in deep tunnels. J Rock Mech Geotech Eng 4(4):289–295

Feng GL, Feng XT, Chen BR, Xiao YX, Zhao ZN (2019) Effects of structural planes on the microseismicity associated with rockburst development processes in deep tunnels of the Jinping-II hydropower station, China. Tunn Undergr Sp Tech 84:273–280

Gutenberg B, Richter CF (1944) Frequency of earthquakes in California. Bull Seismol Soc Am 34(4):185–188

He MC, Xie HP, Peng SP, Jiang YD (2005) Study on rock mechanics in deep mining engineering. Chin J Rock Mech Eng 24(16):2803–2813 (In Chinese)

Jiang FX (2002) Application of microseismic monitoring technology of strata fracturing in underground coal mine. Chin J Geotech Eng 24(2):147–149 (In Chinese)

Kaiser PK, Mccreath DR, Tannant DD (1996) Canadian rockburst support handbook. Laurentian University, Sudbury, Geomechanics Research Centre, p 303

Liu XZ, Tang CA, Li LC, Lv PF, Liu HY (2017) Microseismic monitoring and 3D finite element analysis of the right bank slope, Dagangshan hydropower station, during reservoir impounding. Rock Mech Rock Eng 50(7):1901–1917

Liu F, Tang CA, Ma TH, Tang LX (2019) Characterizing rockbursts along a structural plane in a tunnel of the Hanjiang-to-Weihe River diversion project by microseismic monitoring. Rock Mech Rock Eng 52(6):1835–1856

Legge NB, Spottiswoode SM (1987) Fracturing and microseismicity ahead of a deep gold mine stope in the pre-remnant stages of mining/proceedings of the 6th international congress on rock mechanics. Montreal: [s.n.], p 1071-1078

Tang ZL, Liu XL, Li CY, Qin PX, Xu QJ (2018) Microseismic characteristic analysis in deep TBM construction tunnels. J Tsinghua Univ: Sci & Tech 58(5):461–468 (In Chinese)

Wyss M, Brune JN (2012) Seismic moment, stress, and source dimensions for earthquakes in the California-Nevada region. J Geophys Res 73(14):4681–4694

Wang HL, Ge MC (2008) Acoustic emission/microseismic source location analysis for a limestone mine exhibiting high horizontal stresses. Int J Rock Mech Min Sci 45(5):720–728

Xu NW, Dai F, Liang ZZ, Zhou Z, Sha C, Tang CA (2014) The dynamic evaluation of rock slope stability considering the effects of microseismic damage. Rock Mech Rock Eng 47(2):621–642

Xiao YX, Feng XT, Li SJ, Feng GL, Yu Y (2016) Rock mass failure mechanisms during the evolution process of rockbursts in tunnels. Int J Rock Mech Min Sci 100(83):174–181

Zhang BH, Deng JH, Gao MZ, Zhou ZH, Wu JC, Wu SH (2012) Safety evaluation research based on microseismic monitoring in underground powerhouse of hydropower station. Chin J Rock Mech Eng 31(5):937–944 (In Chinese)

Zhou XP, Peng SL, Zhang JZ, Qian QH, Lu RC (2018) Predictive acoustical behavior of rockburst phenomena in Gaoligongshan tunnel, Dulong river highway, China. Eng Geol 247:117–128